Available online at www.sciencedirect.com
ScienceDirect
Energy Reports 9 (2023) 920–929
www.elsevier.com/locate/egyr

2022 The 3rd International Conference on Power and Electrical Engineering (ICPEE 2022)
29–31 December, Singapore

Impact of DFIG impedance model precision on stability analysis

Tao Xue[a], Ulas Karaagac[a,*], Mohsen Ghafouri[b]

[a] *Department of Electrical Engineering, The Hong Kong Polytechnic University, Hung Hom, Hong Kong Special Administrative Region of China*
[b] *Concordia Institute for Information Systems Engineering (CIISE), Concordia University, Montreal, QC H3G 1M8, Canada*

Received 18 April 2023; accepted 20 May 2023
Available online 7 June 2023

Abstract

Impedance-based stability analysis (IBSA) is an effective method to analyze the interaction problem between the doubly-fed induction generator-based wind park (DFIG-WP) and series compensated or weakly tied AC grids. The analytical impedance model of DFIG has evolved over the years for better precision. This paper presents a precision comparison of those analytical models where the reference is obtained through EMT-level frequency scanning simulations. Moreover, representative IBSA is also performed with those models on typical test systems in which the DFIG adversely interacts with the series compensated grid and weakly tied AC grid in sub- and super-synchronous frequency ranges, respectively. The common modeling approach, which disregards the coupling between the rotor side converter (RSC) and grid side converter (GSC) at the DC-side, reduces the accuracy of IBSA and may lead to incorrect stability analysis results.

Peer-review under responsibility of the scientific committee of the 3rd International Conference on Power and Electrical Engineering, ICPEE, 2022.

Keywords: DFIG; Impedance modeling; Weak grid instability; Series-capacitor SSO; Stability analysis

1. Introduction

With developments of wind turbine (WT) technology in recent years, the wind power penetration level into the power system and the sizes of WTs and wind parks (WPs) have increased significantly. The large-scale WPs implement variable-speed WTs (VSWTs) to increase energy capture, reduce drive train stresses, and comply with grid code requirements [1]. Full-size converter (FSC) and doubly-fed induction generator (DFIG) WTs are typical VSWTs. Recent incidents have shown that VSWTs can interact with the series compensated or weakly tied AC grids in the sub-synchronous frequency range and lead to instability [2]. This phenomenon, which is called sub-synchronous oscillation (SSO), has been widely observed in US, China, and UK [3]. At first, DFIG-based wind parks (DFIG-WPs) are found easily to interact with series-capacitor compensated grids. This phenomenon is called series-capacitor SSO, which is caused by the negative resistance brought by induction generator effect (IGE) [4] and worsened by the converter controls of DFIG (sub-synchronous control interaction, SSCI) [5]. Countermeasures

* Corresponding author.
E-mail address: ulas.karaagac@polyu.edu.hk (U. Karaagac).

https://doi.org/10.1016/j.egyr.2023.05.165

Peer-review under responsibility of the scientific committee of the 3rd International Conference on Power and Electrical Engineering, ICPEE, 2022.

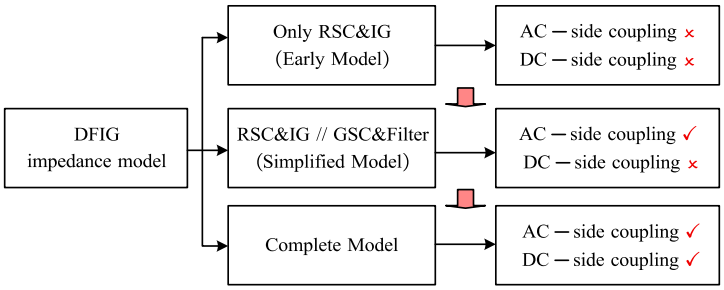

Fig. 1. Flowchart of DFIG impedance model development.

against SSCI includes tuning the control parameters of the rotor side converter (RSC) [6] and implementing damping controllers [7]. Recently, an interaction event between DFIG-WP and weak grid happened in Northwest China [8]. The risk of DFIG weak grid instability has already been demonstrated before this incident and an adaptive grid side converter (GSC) controller has been proposed in [9,10] for mitigation purposes. Impedance-based stability analysis (IBSA) [11] has been widely used for DFIG-WP instability identification and mitigation design [12]. The analytical impedance model of DFIG has evolved over the years due to better precision requirements in IBSA. This development process is shown in Fig. 1. The first DFIG impedance model [13] consists of only series connection of induction generator (IG) and RSC impedance models. The GSC contribution to the DFIG impedance is totally ignored by assuming the total impedance of IG and RSC is dominant, especially in the sub-synchronous frequency range. This model also does not contain the phase-locked loop (PLL) and RSC outer loop controls. The DFIG impedance model is improved by considering the parallel connection of two impedances: (i) IG and RSC impedances, and (ii) GSC and its output filter impedances [14]. Then, this model is refined in [15]. However, the DC bus voltage is assumed to be constant. Therefore, the GSC outer loop controls and DC-side coupling of GSC and RSC are ignored. The DFIG impedance model in [16] represents the DC-side of the GSC with a constant power source in parallel connection with a capacitor, and the DC-side of the RSC with a constant voltage source. Hence, the GSC outer loop control is included but the DC-side coupling of GSC and RSC is still ignored.

Recent studies point out that DC-side impedance can be reflected to AC-side to account for AC-DC couplings and has an impact on DFIG impedance characteristics. In [8,16], the DC-side coupling is accounted by analyzing the disturbance component paths in the DFIG. An equivalent formulation for DC-side coupling is obtained in [17], by keeping the DC-side Kirchhoff's Current Law (KCL) equations in deriving the AC-side impedances. This paper revisits those works and presents an alternative derivation for the complete DFIG impedance model in a more clear and straightforward way. Due to space limitations, the complete DFIG impedance model is compared only with the simplified DFIG impedance model in [18] as the early stage simplified models in [13–15] produce larger errors.

Then, the impacts of AC-DC coupling phenomenon on the DFIG impedance model characteristics and precision of IBSA are discussed. The accuracy of the complete impedance model is demonstrated on typical test systems in which the DFIG adversely interacts with the series compensated grid and weak grid. Furthermore, the weak grid instability is identified at super-synchronous frequency range rather than sub-synchronous range.

The rest of this paper is structured as follows. Section 2 presents the alternative derivations of complete and simplified DFIG impedance models. In Section 3, the precision of those models is compared through electromagnetic transient level (EMT-level) frequency scanning simulations. Section 4 conducts two case studies to illustrate the impact of impedance model precision on IBSA. Section 5 concludes the paper.

2. Impedance modeling of DFIG

2.1. Configurations of the system and the DFIG

The equivalent circuit of the test system is shown in Fig. 2(a) with detailed parameters listed in Table 1. The simulation model contains the aggregated WT model, RL equivalent circuits of WT, and WP transformers referred to low-voltage side, i.e., the WT side. The external grid is represented with parallel RLC circuits behind a voltage source referred to low-voltage side. Opening Switch 1 results in a weak grid condition when Switch 2 is closed.

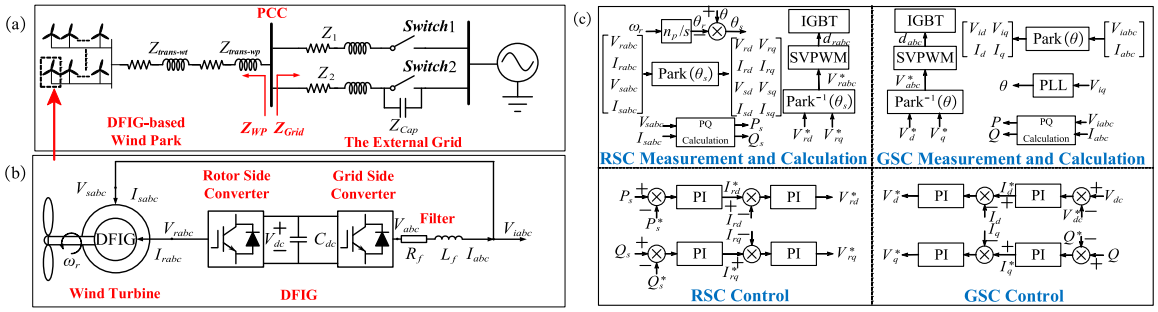

Fig. 2. The system configurations: (a) Circuit diagram of the system, (b) Circuit diagram of the DFIG, and (c) Control diagram of the DFIG.

Table 1. Parameter of the wind park and grid.

Parameters	Value
Equivalent resistance of WT and WP transformers (R_{wt}, R_{wp})	0.002 pu, 0.003 pu
Equivalent reactance of WT and WP transformers (X_{wt}, X_{wp})	0.006 pu, 0.12 pu
Resistance of grid line 1 and 2 (R_{line1}, R_{line2})	0.015 pu, 0.06 pu
Reactance of grid line 1 and 2 (XL_{line1}, XL_{line2}, X_{cap})	0.1 pu, 0.4 pu, 0.12 pu

Table 2. Parameter of the DFIG.

Parameters	Value	
Rated Power and AC volage (S, V_{rms})	2 MW, 690 V	
Stator resistance, leakage, and mutual inductances (R_s, L_{ls}, L_m)	0.0016 Ω, 35.18 mH, 3.6 mH	
Rotor resistance and leakage inductance (R_r, L_{lr})	0.0012 Ω, 15.00 mH	
Pole pairs and rotor angular speed (n_p, ω_r)	2, 1.2 pu	
RSC Current PI regulator (K_{pir}, K_{iir})	0.1120, 15.80 (C1)	0.0427, 1.94 (C2)
RSC Active/Reactive Power PI regulator (K_{ppqr}, K_{ipqr})	0.0002, 0.0368	
GSC DC voltage, DC capacitor and filter (V_{dc}, C_{dc}, R_f, L_f)	1100 V, 10 mF, 0.006 Ω, 37.887 mH	
GSC Current PI regulator (K_{pi}, K_{ii})	0.1636, 35.31 (C1)	0.4907, 317.78 (C2)
GSC PLL Loop filter (PI regulator) (K_{ppll}, K_{ipll})	130, 8388	
GSC DC voltage PI regulator (K_{pvdc}, K_{ivdc})	1.6841, 109.06	
GSC Active/Reactive power PI regulator (K_{pq}, K_{iq})	0.00000840, 0.1584	

Opening Switch 2 results in radial connection of WP to a series capacitor compensated grid (with a 30% effective compensation level) when Switch 1 is open. The circuit and control diagrams of the DFIG are shown in Fig. 2(b) and (c), respectively. The parameters of the DFIG are listed in Table 2. The RSC uses active and reactive power controls at d- and q-axis outer loops, respectively. The GSC uses DC voltage control at d-axis outer loop and reactive power control at q-axis outer loop. The inner control loops of both RSC and GSC use current vector control. Park transformation and its inverse are conducted on the angle provided by PLL.

2.2. Analytical impedance model derivation

2.2.1. Modular multi-terminal impedance models of DFIG submodules

The DFIG is divided into four submodules. The multi-terminal impedance models of each submodule are derived and then assembled according to their electrical connections to obtain the DC- and AC-side impedance models of the DFIG. The impedance model derivation process for DFIG is shown in Fig. 3.

The impedance models of each submodule are built in multi-terminal form first as shown in Fig. 3. Submodule 1 consists of the WT and induction generator (IG). In the electromagnetic transient (EMT) scale, the slow dynamics

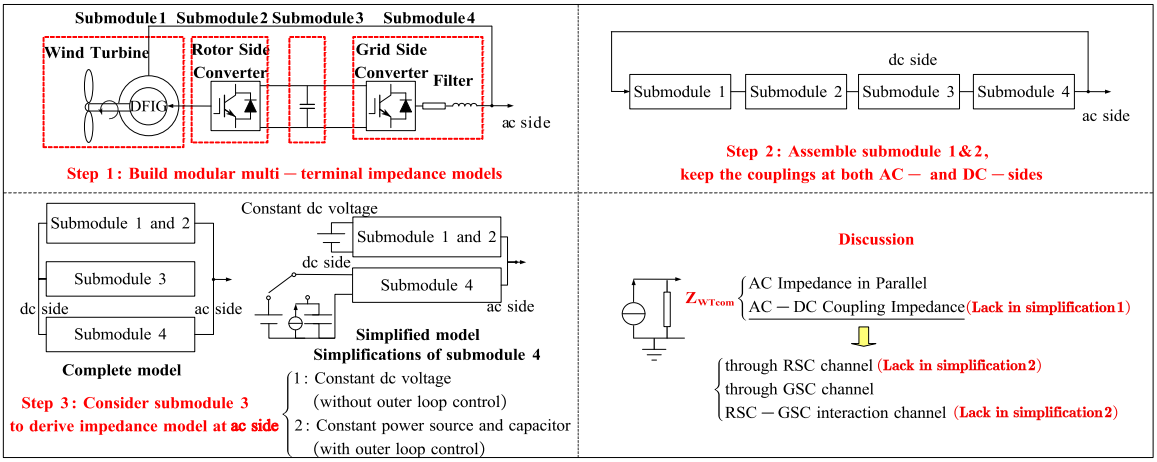

Fig. 3. DFIG impedance modeling procedure.

such as aerodynamics and mechanical characteristics are neglected. Besides, the assumption of constant wind speed is made for a steady operating point so that the modeling process can be simplified. Hence, Submodule 1 contains only the IG and is represented by the following two-terminal impedance model in dq domain:

$$\begin{bmatrix} \widetilde{V}^s_{1d} & \widetilde{V}^s_{1q} & \widetilde{V}^s_{2d} & \widetilde{V}^s_{2q} \end{bmatrix}^T = \begin{bmatrix} \mathbf{Z_{ls}} & \mathbf{Z_{lm}} \\ \mathbf{Z_{lmslip}} & \mathbf{Z_{lr}} \end{bmatrix} \begin{bmatrix} \widetilde{I}^s_{1d} & \widetilde{I}^s_{1q} & \widetilde{I}^s_{2d} & \widetilde{I}^s_{2q} \end{bmatrix}^T \tag{1}$$

The stator voltages and currents are marked with subscripts '1' (V_{1d}, V_{1q}, I_{1d} and I_{1q}), and the rotor voltages and currents are marked with subscripts '2' (V_{2d}, V_{2q}, I_{2d} and I_{2q}). The currents flowing into the stator and rotor are marked as positive direction (motor convention). In this paper, a variable with a tilde indicates the small signal form and a bold letter denotes a matrix. Superscripts 's' and 'c' indicate the variables at electrical- and control-side coordinates, respectively. The electrical- and control-side coordinates are different due to PLL influence.

The voltage and current equations of submodule 2 (RSC) are:

$$\begin{bmatrix} -\widetilde{I}^s_{2d} & -\widetilde{I}^s_{2q} & \widetilde{I}_{2dc} \end{bmatrix}^T = \begin{bmatrix} \mathbf{Y_{2dq}} & \mathbf{Y_{2a}} \\ \mathbf{Y_{2b}} & Y_{2dc} \end{bmatrix} \begin{bmatrix} \widetilde{V}^s_{2d} & \widetilde{V}^s_{2q} & \widetilde{V}_{2dc} \end{bmatrix}^T \tag{2}$$

$\mathbf{Y_{2dq}}$ is a 2 by 2 AC self-admittance matrix and Y_{2dc} is the DC self-admittance. $\mathbf{Y_{2a}}$ is the mutual admittance between DC voltage V_{2dc} and AC currents I_{2dq}.$\mathbf{Y_{2b}}$ is the mutual admittance between AC voltages V_{2dq} and DC current I_{2dc}.

The dynamics of submodule 3 (DC bus capacitor) can be represented by a KCL equation as:

$$\widetilde{I}_{2dc} + \widetilde{I}_{4dc} + sC_{dc}\widetilde{V}_{3dc} = 0 \tag{3}$$

The letter s is the Laplace operator, and the DC bus capacitance and voltage are C_{dc} and V_{3dc}, respectively.

The voltage and current equations of submodule 4 (GSC and the L-type filter) are:

$$\begin{bmatrix} -\widetilde{I}^s_{4d} & -\widetilde{I}^s_{4q} & \widetilde{I}_{4dc} \end{bmatrix}^T = \begin{bmatrix} \mathbf{Y_{4dq}} & \mathbf{Y_c} \\ \mathbf{Y_d} & Y_{4dc} \end{bmatrix} \begin{bmatrix} \widetilde{V}^s_{4id} & \widetilde{V}^s_{4iq} & \widetilde{V}_{4dc} \end{bmatrix}^T \tag{4}$$

V_{4id}, V_{4iq} are the DFIG AC-side voltages and I_{4d}, I_{4q} are the GSC currents. V_{4dc} and I_{4dc} are the voltage and current at GSC DC-side. $\mathbf{Y_{4dq}}$ is the 2 by 2 AC self-admittance matrix and Y_{4dc} is the DC self-admittance. Moreover, $\mathbf{Y_c}$ is the mutual admittance between DC voltage V_{4dc} and AC currents I_{4dq}. $\mathbf{Y_d}$ is the mutual admittance between AC voltages V_{4idq} and DC current I_{4dc}.

2.2.2. General solution

Step-2 is to assemble submodule 1 and 2 based on the equivalence of rotor and RSC variables. Modify (2) with (1) by canceling V_{2dq} and I_{2dq}:

$$\begin{bmatrix} \widetilde{I}^s_{1d} & \widetilde{I}^s_{1q} & \widetilde{I}_{2dc} \end{bmatrix}^T = \begin{bmatrix} \mathbf{Y_{12dq}} & \mathbf{Y_a} \\ \mathbf{Y_b} & Y_{2dc} \end{bmatrix} \begin{bmatrix} \widetilde{V}^s_{1d} & \widetilde{V}^s_{1q} & \widetilde{V}_{2dc} \end{bmatrix}^T \tag{5}$$

The KCL and Kirchhoff's Voltage Law (KVL) equations of submodule 3 and DFIG AC-side are:

$$dc\begin{cases} sC_{dc}\widetilde{V_{dc}} = -\widetilde{I_{2dc}} - \widetilde{I_{4dc}} \quad (a) \\ \widetilde{V_{dc}} = \widetilde{V_{2dc}} = \widetilde{V_{3dc}} = \widetilde{V_{4dc}} \end{cases} \qquad ac\begin{cases} \begin{bmatrix} \widetilde{I_{WTd}} & \widetilde{I_{WTq}} \end{bmatrix}^T = \begin{bmatrix} \widetilde{I^s_{1d}} - \widetilde{I^s_{4d}} & \widetilde{I^s_{1q}} - \widetilde{I^s_{4q}} \end{bmatrix}^T \\ \begin{bmatrix} \widetilde{V_{WTd}} & \widetilde{V_{WTq}} \end{bmatrix}^T = \begin{bmatrix} \widetilde{V^s_{1d}} & \widetilde{V^s_{1q}} \end{bmatrix}^T = \begin{bmatrix} \widetilde{V^s_{4id}} & \widetilde{V^s_{4iq}} \end{bmatrix}^T \end{cases} (b) \tag{6}$$

The subscript 'WT' means variables at DFIG output terminal (AC-side). It is essential to keep (6) in the derivation process so that the couplings at AC- and DC-sides can be represented.

Step-3 is to derive the AC-side impedance while keeping the relationship of (6). Substituting the third rows of (4) and (5) into (6)(a), we can obtain:

$$sC_{dc}\widetilde{V_{dc}} = -\left(\mathbf{Y_b} + \mathbf{Y_d}\right)\begin{bmatrix} \widetilde{V_{WTd}} & \widetilde{V_{WTq}} \end{bmatrix}^T - \left(Y_{2dc} + Y_{4dc}\right)\widetilde{V_{dc}} \tag{7}$$

The DC-side voltage is coupled with the AC-side voltage in (7). Then, substituting (6)(b) into the sum of the first two rows of (4) and (5) yields:

$$\begin{bmatrix} \widetilde{I_{WTd}} & \widetilde{I_{WTq}} \end{bmatrix}^T = \left(\mathbf{Y_{12dq}} + \mathbf{Y_{4dq}}\right)\begin{bmatrix} \widetilde{V_{WTd}} & \widetilde{V_{WTq}} \end{bmatrix}^T + \left(\mathbf{Y_a} + \mathbf{Y_c}\right)\widetilde{V_{dc}} \tag{8}$$

The DC-side voltage is coupled with AC-side current and voltage in (8). Then, the DFIG impedance model is obtained by canceling the DC-side voltage of (7) and (8):

$$\begin{bmatrix} \widetilde{I_{WTd}} & \widetilde{I_{WTq}} \end{bmatrix}^T = \mathbf{Z_{WTcom}}^{-1}\begin{bmatrix} \widetilde{V_{WTd}} & \widetilde{V_{WTq}} \end{bmatrix}^T \quad \mathbf{Z_{WTcom}} = \left[\mathbf{Y_{12dq}} + \mathbf{Y_{4dq}} - \frac{\left(\mathbf{Y_a} + \mathbf{Y_c}\right)\left(\mathbf{Y_b} + \mathbf{Y_d}\right)}{sC_{dc} + Y_{2dc} + Y_{4dc}}\right]^{-1} \tag{9}$$

Simplification of the GSC DC-side has two options: one option is a constant DC voltage source, whereas the other one is a constant power source and a capacitor in parallel. The first ignores all the AC-DC coupling so it is more inaccurate, which will not be discussed in this paper. The second keeps the AC-DC coupling through the GSC; thus, this simplification has better accuracy and will be compared with the complete model. The matrices need to be modified if simplification 2 is done:

$$\mathbf{Z_{WTsim}} = \left[\mathbf{Y_{12dq}} + \mathbf{Y_{4dq}} - \mathbf{Y_c}\mathbf{Y_d}/\left(C_{dc} - P_r/V_{dc}^2 + Y_{4dc}\right)\right]^{-1} \tag{10}$$

2.2.3. Particular solution for RSC and IG

The particular solution is obtained by introducing equations of the controller, machine, filter and power balance into the general solution. The Eq. (1) of submodule 1 is rewritten considering the machine equations:

$$\begin{bmatrix} \widetilde{V^s_{1d}} \\ \widetilde{V^s_{1q}} \\ \widetilde{V^s_{2d}} \\ \widetilde{V^s_{2q}} \end{bmatrix} = \begin{bmatrix} \underbrace{\begin{matrix} R_s + sL_{sd} & -\omega L_{sq} \\ \omega L_{sd} & R_s + sL_{sq} \end{matrix}}_{\mathbf{Z_{ls}}} & \underbrace{\begin{matrix} sL_m & -\omega L_m \\ \omega L_m & sL_m \end{matrix}}_{\mathbf{Z_{lm}}} \\ \underbrace{\begin{matrix} sL_m & -\omega_{slip} L_m \\ \omega_{slip} L_m & sL_m \end{matrix}}_{\mathbf{Z_{lmslip}}} & \underbrace{\begin{matrix} R_r + sL_{rd} & -\omega_{slip} L_{rq} \\ \omega_{slip} L_{rd} & R_r + sL_{rq} \end{matrix}}_{\mathbf{Z_{lr}}} \end{bmatrix} \begin{bmatrix} \widetilde{I^s_{1d}} \\ \widetilde{I^s_{1q}} \\ \widetilde{I^s_{2d}} \\ \widetilde{I^s_{2q}} \end{bmatrix} \tag{11}$$

R_s, L_{sd}, and L_{sq} are stator resistance, d- and q-axis inductances, respectively. L_{ls} is the stator leakage inductance and L_m is the mutual inductance. R_r, L_{rd}, and L_{rq} are rotor resistance, d- and q-axis inductances, respectively. ω and ω_{slip} are fundamental and slip frequencies.

The first two rows of Eq. (5) is modified according to the RSC inner and outer loop controls:

$$\begin{bmatrix} I_{2dref} \\ I_{2qref} \end{bmatrix} = \left(K_{ppqr} + \frac{K_{ipqr}}{s}\right)\begin{bmatrix} 1.5\left(V^s_{sd}I^s_{sd} + V^s_{sq}I^s_{sq}\right) - P_{ref} \\ 1.5\left(V^s_{sd}I^s_{sq} - V^s_{sq}I^s_{sd}\right) - Q_{ref} \end{bmatrix} = H_{pqr}\begin{bmatrix} 1.5\left(V^s_{sd}I^s_{sd} + V^s_{sq}I^s_{sq}\right) - P_{ref} \\ 1.5\left(V^s_{sd}I^s_{sq} - V^s_{sq}I^s_{sd}\right) - Q_{ref} \end{bmatrix} \tag{12}$$

$$\begin{bmatrix} V^c_{rd} \\ V^c_{rq} \end{bmatrix} = \frac{V_{2dc}/2}{V_{2dc0}/2}\left(K_{pir} + \frac{K_{iir}}{s}\right)\begin{bmatrix} I_{2dref} - I^c_{2d} \\ I_{2qref} - I^c_{2q} \end{bmatrix} = \frac{V_{2dc}/2}{V_{2dc0}/2}H_{cr}\begin{bmatrix} I_{2dref} - I^c_{2d} \\ I_{2qref} - I^c_{2q} \end{bmatrix} \tag{13}$$

In these equations, K_{ppqr}, K_{ipqr} and K_{pir}, K_{iir} are proportional and integral parameters of the outer and inner loop PI controllers. In Eq. (13), the numerator represents switching of the IGBTs, and the denominator represents

uniformization before the space vector pulse width modulation (SVPWM). The small signal RSC variables are expressed in the control-side coordinates and need to be transformed into electrical-side coordinates [19]:

$$\begin{bmatrix} \widetilde{V_{2d}^c} & \widetilde{V_{2q}^c} & \widetilde{I_{2d}^c} & \widetilde{I_{2q}^c} \end{bmatrix}^T = \begin{bmatrix} \widetilde{V_{2d}^s} & \widetilde{V_{2q}^s} & \widetilde{I_{2d}^s} & \widetilde{I_{2q}^s} \end{bmatrix}^T + \begin{bmatrix} \mathbf{G_{Vrpll}} & \mathbf{G_{Irpll}} \end{bmatrix}^T \begin{bmatrix} \widetilde{V_{1d}^s} & \widetilde{V_{1q}^s} \end{bmatrix}^T$$
$$\mathbf{G_{Vrpll}} = \begin{bmatrix} 0 & V_{2q}^s G_{pll} \\ 0 & -V_{2d}^s G_{pll} \end{bmatrix} \quad \mathbf{G_{Irpll}} = \begin{bmatrix} 0 & I_{2q}^s G_{pll} \\ 0 & -I_{2d}^s G_{pll} \end{bmatrix} \quad G_{pll} = \frac{K_{pll}+K_{ipll}/s}{V_{1d}^s(s+K_{pll}+K_{ipll}/s)} \tag{14}$$

where K_{ppll} and K_{ipll} are the PI parameters of the PLL.

Substituting (11) and (14) into the linearized versions of (12) and (13) to cancel V_{2d}, V_{2q}, I_{2d} and I_{2q} yields $\mathbf{Y_{12dq}}$ and $\mathbf{Y_a}$, where $\mathbf{I}$ is the identity matrix.

$$\mathbf{Y_{12dq}} = \mathbf{A_r^{-1}B_r} \quad , \quad \mathbf{Y_a} = -\mathbf{A_r^{-1}} \begin{bmatrix} V_{2d}^s & V_{2q}^s \end{bmatrix}^T / V_{dc}$$
$$\mathbf{A_r} = H_{cr} 1.5 H_{pqr} \begin{bmatrix} V_{1d}^s & V_{1q}^s \\ -V_{1q}^s & V_{1d}^s \end{bmatrix} + (H_{cr}\mathbf{I} + \mathbf{Z_{lr}})\mathbf{Z_{lm}^{-1}}\mathbf{Z_{ls}} - \mathbf{Z_{lmslip}}$$
$$\mathbf{B_r} = (H_{cr}\mathbf{I} + \mathbf{Z_{lr}})\mathbf{Z_{lm}^{-1}} + H_{cr}\left(-1.5 H_{pqr} \begin{bmatrix} I_{1d}^s & I_{1q}^s \\ -I_{1q}^s & I_{1d}^s \end{bmatrix} + \mathbf{G_{Irpll}}\right) + \mathbf{G_{Vrpll}} \tag{15}$$

The third row of (5) is modified according to the power balance between RSC and DC bus:

$$I_{2dc} = 1.5\left(V_{2d}^s I_{2d}^s + V_{2q}^s I_{2q}^s\right) / \left(V_{2dc}\right) \tag{16}$$

Substituting (11) and (15) into the linearized version of (16) yields $\mathbf{Y_b}$ and Y_{2dc}:

$$\begin{aligned} \mathbf{Y_b} &= 1.5\begin{bmatrix} I_{2d}^s & I_{2q}^s \end{bmatrix}\left[\mathbf{Z_{lmslip}} - \mathbf{Z_{lr}}\mathbf{Z_{lm}^{-1}}\mathbf{Z_{ls}}\right]\mathbf{Y_{12dq}}/V_{dc} - 1.5\begin{bmatrix} V_{2d}^s & V_{2q}^s \end{bmatrix}\mathbf{Z_{lm}^{-1}}\mathbf{Z_{ls}}\mathbf{Y_{12dq}}/V_{dc} \\ &\quad +1.5\left\{\begin{bmatrix} I_{2d}^s & I_{2q}^s \end{bmatrix}\mathbf{Z_{lr}}\mathbf{Z_{lm}^{-1}} + \begin{bmatrix} V_{2d}^s & V_{2q}^s \end{bmatrix}\mathbf{Z_{lm}^{-1}}\right\}/V_{dc} \\ Y_{2dc} &= 1.5\begin{bmatrix} I_{2d}^s & I_{2q}^s \end{bmatrix}\left[\mathbf{Z_{lmslip}} - \mathbf{Z_{lr}}\mathbf{Z_{lm}^{-1}}\mathbf{Z_{ls}}\right]\mathbf{Y_a}/V_{dc} - 1.5\begin{bmatrix} V_{2d}^s & V_{2q}^s \end{bmatrix}\mathbf{Z_{lm}^{-1}}\mathbf{Z_{ls}}\mathbf{Y_a}/V_{dc} - P_r/V_{dc}^2 \end{aligned} \tag{17}$$

2.2.4. Particular solution for GSC and filter

Derivation of GSC is similar to grid-tied voltage source converter (VSC) and the final equations of $\mathbf{Y_{4dq}}$, $\mathbf{Y_c}$, $\mathbf{Y_d}$ and Y_{4dc} are given below. Reader should refer to [20] for details.

$$\mathbf{Y_{4dq}}=\mathbf{A^{-1}BY_c}=\mathbf{A^{-1}C}$$
$$\mathbf{A} = H_c\mathbf{I} + \mathbf{Z_{fdq}} - H_c 1.5 H_q \begin{bmatrix} 0 & 0 \\ V_{4iq}^s & -V_{4id}^s \end{bmatrix} \quad \mathbf{B} = \mathbf{I} + H_c\mathbf{G_{Ipll}} + \mathbf{G_{Vpll}} - H_c H_q 1.5 H_q \begin{bmatrix} 0 & 0 \\ I_{4q}^s & -I_{4d}^s \end{bmatrix}$$
$$\mathbf{C} = -H_c\begin{bmatrix} H_{dc} & 0 \end{bmatrix}^T - \begin{bmatrix} V_{4d}^s/V_{dc} & V_{4q}^s/V_{dc} \end{bmatrix}^T \tag{18}$$

$$\mathbf{Y_d}=\mathbf{D} - \mathbf{EA^{-1}B} \quad Y_{4dc} = F - \mathbf{EA^{-1}C}$$
$$\mathbf{D} = 1.5\begin{bmatrix} I_{4d}^s & I_{4q}^s \end{bmatrix}/V_{dc} \quad \mathbf{E} = 1.5\left\{\begin{bmatrix} V_{4d}^s & V_{4q}^s \end{bmatrix} + \begin{bmatrix} I_{4d}^s & I_{4q}^s \end{bmatrix}\mathbf{Z_{fdq}}\right\}/V_{dc} \quad F = -P_r/V_{dc}^2 \tag{19}$$

Finally, substituting $\mathbf{Y_{12dq}}$, $\mathbf{Y_a}$ of (15), $\mathbf{Y_b}$, Y_{2dc} of (17), $\mathbf{Y_{4dq}}$, $\mathbf{Y_c}$ of (18) and $\mathbf{Y_d}$, Y_{4dc} of (19) into $\mathbf{Z_{WTcom}}$ in (9) and $\mathbf{Z_{WTsim}}$ in (10), we can obtain the DFIG complete and simplified impedance models.

3. Comparison of impedance models

The DFIG dq MIMO impedance ($\mathbf{Z_{WTcom}}$ and $\mathbf{Z_{WTsim}}$) are transformed into SISO sequence impedance (Z_{WTcom} and Z_{WTsim}) according to [21] and compared with the EMT-level impedance scan. The DFIG control parameters are designed as follows. The RSC controller is designed considering only the IG parameters, which are R_s, L_{ls}, R_r, L_{lr} and L_m. The GSC controller is designed considering the equivalent impedance seen from the converter terminal of the aggregated DFIG [22]. Accounting external grid in GSC controller design ensures stable operation when it is connected to a weak grid [9,10]. Further details can be found in [23]. The PI regulator parameters of the inner and outer controls (seen in Table 2) are similar to the ones in [24], which successfully imitated the actual transient behavior of a DFIG-WP. Fig. 4 confirms the complete impedance model accuracy. The error of

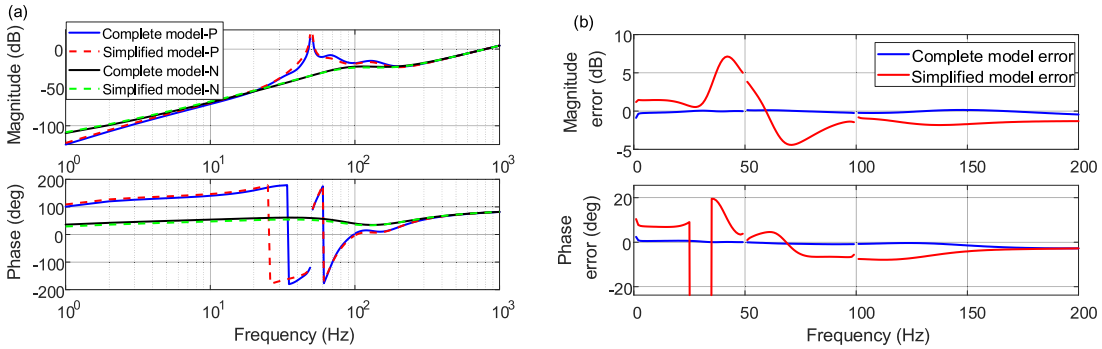

Fig. 4. Verification of impedance models of the DFIG: (a) positive sequence impedances, and (b) errors compared to the frequency scan.

the simplified model mainly exists in 0 Hz–200 Hz range and may affect the IBSA accuracy. Explanations of the simplified model discrepancies are discussed briefly here and need further investigation in future work. Splitting the terms in (9) shows the formation of the AC-side DFIG admittance:

$$\begin{aligned}\mathbf{Y_{WTcom}} &= \mathbf{Y_{12dq}} + \mathbf{Y_{4dq}}\,(\text{AC admittances}) - \mathbf{Y_a Y_b} Z_{dc}\,(\text{RSC channel})\\ &\quad -\mathbf{Y_c Y_d} Z_{dc}\,(\text{GSC channel}) - (\mathbf{Y_a Y_c} + \mathbf{Y_b Y_d})\, Z_{dc}\,(\text{RSC} - \text{GSC interaction channel})\\ Z_{dc} &= 1/\,(sC_{dc} + Y_{2dc} + Y_{4dc})\end{aligned} \tag{20}$$

As seen in (20), the AC-side DFIG admittance contains two AC terms and three AC–DC coupling terms. $\mathbf{Y_{12dq}} + \mathbf{Y_{4dq}}$ is the sum of RSC and GSC AC self-admittances. $\mathbf{Y_a}$ and $\mathbf{Y_b}$ are mutual admittances in submodules 1 and 2 (see (5)), and contribute to the coupling channel via RSC. $\mathbf{Y_c}$ and $\mathbf{Y_d}$ are mutual admittances in submodule 4 (see (4)), and contribute to the coupling channel via GSC. The term $\mathbf{Y_a Y_c} + \mathbf{Y_b Y_d}$ contributes to the coupling channel through the interaction of RSC and GSC. Simplified model in (10) ignores the coupling channels through RSC and RSC-GSC interaction. In addition, Y_{2dc} is also simplified to a constant power source.

4. Illustrative case studies

4.1. Case 1: Impact of impedance model accuracy on weak grid instability analysis

In case 1 (C1), Switches 1 and 2 are initially closed. At t = 1 s, Switch 1 opens and a weak grid condition is formed. The IBSA with the complete impedance model ($Z_{WPcom} = Z_{WTcom} + Z_{trans-wt} + Z_{trans-wp}$) indicates a stable system with 76.7 Hz intersection frequency and 10.4° phase margin as shown in Fig. 5. However, with the simplified impedance model ($Z_{WPsim} = Z_{WTsim} + Z_{trans-wt} + Z_{trans-wp}$), IBSA indicates an unstable system with 76.1 Hz intersection frequency and −0.8° phase margin. The stable operation is confirmed with EMT simulations as shown in Fig. 6. The simplified model usage in IBSA may lead to incorrect conclusion especially when the system has a small stability margin. Although weak grid instability is classified as SSO, the resonance frequency is at super-synchronous range. Further research is needed to investigate the resonance frequency range of the instability phenomenon resulted from interactions of DFIG with a weakly tied AC grid.

4.2. Case 2: Impact of impedance model accuracy on series-capacitor SSO

In case 2 (C2), initially, Switch 1 is closed and Switch 2 is open. At t = 1 s, Switch 1 opens, and series-capacitor compensated grid condition is formed. The IBSA with the complete impedance model (Z_{WPcom}) indicates a stable system with 15.6 Hz intersection frequency and 2.6° phase margin as shown in Fig. 7. However, with the simplified impedance model (Z_{WPsim}), IBSA indicates an unstable system with 15.1 Hz intersection frequency and −1.7° phase margin. The stable operation is confirmed with EMT simulations as shown in Fig. 8. The discrepancy of the simplified model compared to the complete model is smaller in C2 (0.5 Hz = 15.6 Hz–15.1 Hz, and 4.3° = 2.6° - (−1.7°)) than in C1 (0.6 Hz = 76.7 Hz–76.1 Hz, and 11.2° = 10.4° - (−0.8°)), because the error of the simplified model is more significant in 70 Hz–80 Hz range than in 10 Hz–20 Hz range as shown in Fig. 4(b).

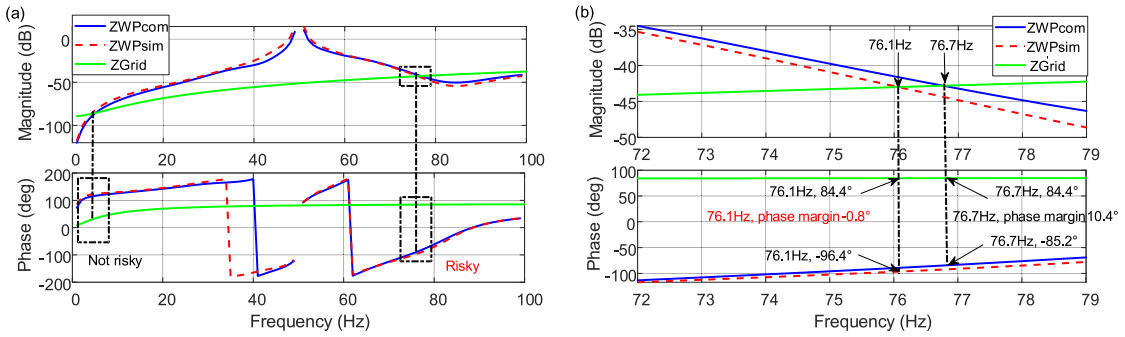

Fig. 5. IBSA of C1: (a) Bode diagram, and (b) Zoom-in view of risky frequency range in the Bode diagram.

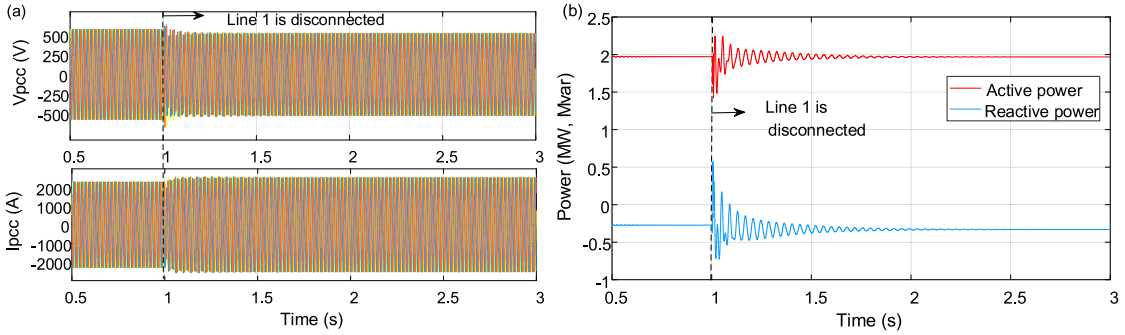

Fig. 6. EMT simulation of C1: (a) PCC voltages and currents, and (b) PCC power.

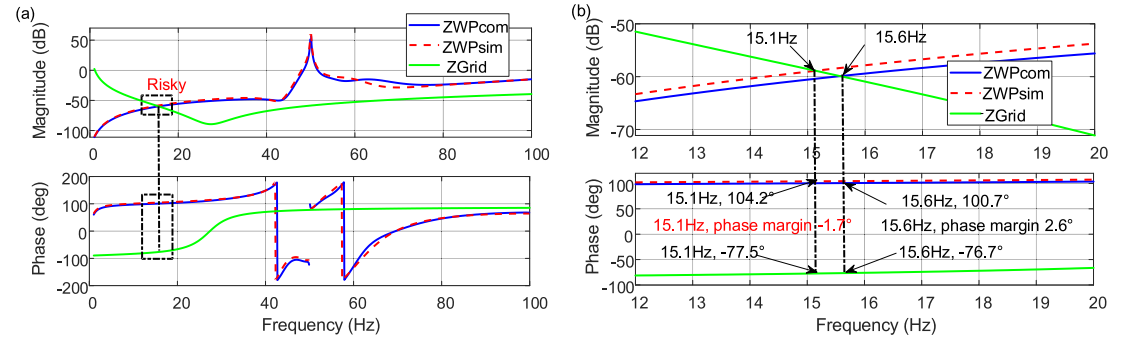

Fig. 7. IBSA of C2: (a) Bode diagram, and (b) Zoom-in view of risky frequency range in the Bode diagram.

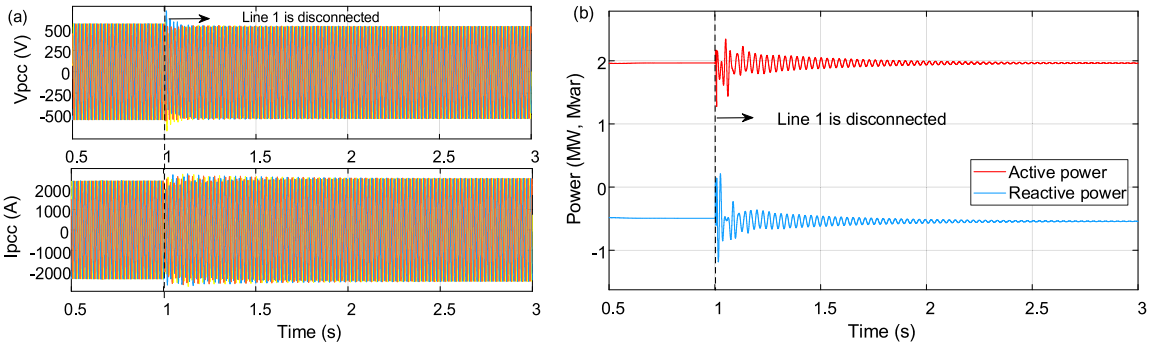

Fig. 8. EMT simulation of C2: (a) PCC voltages and currents, and (b) PCC power.

5. Conclusions

This paper presented an alternative derivation for the complete DFIG impedance model. The complete impedance modeling of the DFIG includes both AC impedances and AC-DC coupling impedances. The DC- and AC-sides are coupled through RSC, GSC, and RSC-GSC interaction channels. The simplified models ignore some of the channels to different extents. This paper also demonstrated the impact of AC–DC coupling phenomenon on DFIG impedance characteristics and IBSA precision on typical test systems in which the DFIG adversely interacts with the series compensated grid and weakly tied AC grid, respectively. The simplified model used in IBSA may lead to an incorrect conclusion, especially when the system has a small stability margin. The weak grid instability is identified at super-synchronous range although typically expected in sub-synchronous range. Moreover, this classification might be due to a misperception. The reasons might include dq reference frame usage in analytical analysis, availability of only RMS measurements or presence of relatively large mirror frequency components in some of the real-life incidents. Further research is needed to investigate the resonance frequency range of DFIG weak grid instability phenomenon.

Declaration of competing interest

The authors declare the following financial interests/personal relationships which may be considered as potential competing interests: Ulas Karaagac reports financial support was provided by Hong Kong Research Grant Council for the Research Project under Grant 25223118.

Data availability

No data was used for the research described in the article.

Acknowledgment

This work was supported by the Hong Kong Research Grant Council for the Research Project under Grant 25223118.

References

[1] B. Wu, Y. Lang, N. Zargari, S. Kouro, Power conversion and control of wind energy systems, IEEE Press, Wiley, Hoboken, N.J, 2011.
[2] IEEE PES WindSSO Taskforce, PES TR-80: Wind energy systems subsynchronous oscillations: Events and modeling, 2020, https://resourcecenter.ieee-pes.org/publications/technical-reports/PES TP TR80 AMPS WSSO 070920.html.
[3] Y. Cheng, et al., Real-world subsynchronous oscillation events in power grids with high penetrations of inverter-based resources, IEEE Trans Power Syst 38 (1) (2023) 316–330.
[4] L. Fan, Z. Miao, Nyquist-stability-criterion-based SSR explanation for type-3 wind generators, IEEE Trans Energy Convers 27 (3) (2012) 807–809.
[5] G.D. Irwin, A.K. Jindal, A.L. Isaacs, Sub-synchronous control interactions between type 3 wind turbines and series compensated AC transmission systems, in: IEEE power and energy society general meeting, 2011.
[6] U. Karaagac, J. Mahseredjian, S. Jensen, R. Gagnon, M. Fecteau, I. Kocar, Safe operation of DFIG-based wind parks in series-compensated systems, IEEE Trans Power Deliv 33 (2) (2018) 709–718.
[7] M. Ghafouri, U. Karaagac, J. Mahseredjian, H. Karimi, SSCI damping controller design for series-compensated DFIG-based wind parks considering implementation challenges, IEEE Trans Power Syst 34 (4) (2019) 2644–2653.
[8] J. Sun, I. Vieto, Development and application of type-III turbine impedance models including DC bus dynamics, IEEE Open J Power Electron 1 (2020) 513–528.
[9] L.J. Cai, I. Erlich, U. Karaagac, J. Mahseredjian, Stable operation of doubly-fed induction generator in weak grids, in: IEEE power and energy society general meeting, vol. 2015-September, 2015.
[10] L.J. Cai, I. Erlich, Doubly fed induction generator controller design for the stable operation in weak grids, IEEE Trans Sustain Energy 6 (3) (2015) 1078–1084.
[11] J. Sun, Impedance-based stability criterion for grid-connected inverters, IEEE Trans Power Electron 26 (11) (2011) 3075–3078.
[12] J. Shair, X. Xie, G. Yan, Mitigating subsynchronous control interaction in wind power systems: Existing techniques and open challenges, Renew Sustain Energy Rev 108 (2019) 330–346.
[13] Z. Miao, Impedance-model-based SSR analysis for type 3 wind generator and series-compensated network, IEEE Trans Energy Convers 27 (4) (2012) 984–991.
[14] I. Vieto, J. Sun, Impedance modeling of doubly-fed induction generators, in: 2015 17th European conference on power electronics and applications, 2015.
[15] I. Vieto, J. Sun, Sequence impedance modeling and analysis of type-III wind turbines, IEEE Trans Energy Convers 33 (2) (2018) 537–545.

[16] I. Vieto, G. Li, J. Sun, Behavior, modeling and damping of a new type of resonance involving type-III wind turbines, in: 2018 IEEE 19th workshop on control and modeling for power electronics, 2018, pp. 1–8.
[17] C. Zhang, X. Cai, M. Molinas, A. Rygg, Frequency-domain modeling and stability analysis of a DFIG-based wind energy conversion system under non-compensated AC grids: impedance modeling effects and consequences on stability, IET Power Electron 12 (4) (2019) 907–914.
[18] L. Chen, H. Nian, Y. Xu, Complex transfer function-based sequence domain impedance model of doubly fed induction generator, IET Renew Power Gener 13 (1) (2019) 67–77.
[19] B. Wen, D. Dong, D. Boroyevich, R. Burgos, P. Mattavelli, Z. Shen, Impedance-based analysis of grid-synchronization stability for three-phase paralleled converters, IEEE Trans Power Electron 31 (1) (2016) 26–38.
[20] T. Xue, J. Lyu, Y. Li, H. Wang, X. Cai, A comprehensive study on impedance models of grid-tied voltage-source converters, in: IECON proceedings (Industrial electronics conference), 2020, pp. 3118–3125.
[21] A. Rygg, M. Molinas, C. Zhang, X. Cai, A modified sequence-domain impedance definition and its equivalence to the dq-domain impedance definition for the stability analysis of AC power electronic systems, IEEE J Emerg Sel Top Power Electron 4 (4) (2016) 1383–1396.
[22] R. Pena, J.C. Clare, G.M. Asher, Doubly fed induction generator using back to back PWM converters and its application to variable-speed wind-energy generation, IEE Proc Electr Power Appl 143 (3) (1996) 231–240.
[23] Y. Seyedi, U. Karaagac, J. Mahseredjian, A. Haddadi, K. Jacobs, H. Karimi, Detailed modeling of inverter-based resources, in: F. Milano (Ed.), Advances in power system modeling, control and stability analysis, 2nd ed. IET Energy Engineering, 2022, pp. 175–203 [Chapter 5].
[24] A. Haddadi, I. Kocar, T. Kauffmann, U. Karaagac, E. Farantatos, J. Mahseredjian, Field validation of generic wind park models using fault records, J Mod Power Syst Clean Energy 7 (4) (2019) 826–836.